CrossMark

Advanced ACTPol Low-Frequency Array: Readout and Characterization of Prototype 27 and 39 GHz Transition Edge Sensors

B. J. Koopman[1] · N. F. Cothard[2] · S. K. Choi[3] · K. T. Crowley[3] ·
S. M. Duff[4] · S. W. Henderson[5] · S. P. Ho[3] · J. Hubmayr[4] ·
P. A. Gallardo[1] · F. Nati[6] · M. D. Niemack[1] · S. M. Simon[7] · S. T. Staggs[3] ·
J. R. Stevens[1] · E. M. Vavagiakis[1] · E. J. Wollack[8]

Abstract Advanced ACTPol (AdvACT) is a third-generation polarization upgrade to the Atacama Cosmology Telescope, designed to observe the cosmic microwave background (CMB). AdvACT expands on the 90 and 150 GHz transition edge sensor (TES) bolometer arrays of the ACT Polarimeter (ACTPol), adding both high-frequency (HF, 150/230 GHz) and low-frequency (LF, 27/39 GHz) multichroic arrays. The addition of the high- and low-frequency detectors allows for the characterization of synchrotron and spinning dust emission at the low frequencies and foreground emission from galactic dust and dusty star-forming galaxies at the high frequencies. The increased spectral coverage of AdvACT will enable a wide range of CMB science, such as improving constraints on dark energy, the sum of the neutrino masses, and the existence of primordial gravitational waves. The LF array will be the final AdvACT array, replacing one of the MF arrays for a single season. Prior to the fabrication of the final LF detector array, we designed and characterized prototype TES bolometers. Detector geometries

✉ B. J. Koopman
bjk98@cornell.edu

1   Department of Physics, Cornell University, Ithaca, NY 14853, USA

2   Department of Applied and Engineering Physics, Cornell University, Ithaca, NY 14853, USA

3   Joseph Henry Laboratories of Physics, Jadwin Hall, Princeton University, Princeton, NJ 08544, USA

4   NIST Quantum Devices Group, 325 Broadway Mailcode 817.03, Boulder, CO 80305, USA

5   SLAC National Accelerator Laboratory, Kavli Institute for Particle Astrophysics and Cosmology, 2575 Sand Hill Rd, Menlo Park, CA 94025, USA

6   Department of Physics and Astronomy, University of Pennsylvania, 209 South 33rd Street, Philadelphia, PA 19104, USA

7   Department of Physics, University of Michigan, Ann Arbor 48103, USA

8   NASA Goddard Space Flight Center, Greenbelt, MD 20771, USA

in these prototypes are varied in order to inform and optimize the bolometer designs for the LF array, which requires significantly lower noise levels and saturation powers (as low as $\sim 1\,\mathrm{pW}$) than the higher-frequency detectors. Here we present results from tests of the first LF prototype TES detectors for AdvACT, including measurements of the saturation power, critical temperature, thermal conductance, and time constants. We also describe the modifications to the time-division SQUID readout architecture compared to the MF and HF arrays.

Keywords Cosmic microwave background · Transition edge sensor · Bolometer · Polarimetry · Advanced ACTPol · Synchrotron

1 Introduction

Advanced ACTPol (AdvACT) is an upgrade to the Atacama Cosmology Telescope polarimeter (ACTPol), designed to observe the polarization of the cosmic microwave background (CMB) across five different frequency bands [1]. ACT is an off-axis Gregorian telescope located in the Chilean Atacama Desert at an elevation of 5190 m [2]. The telescope optical chain consists of a 6-m-diameter primary mirror, a 2-m-diameter secondary mirror, and a set of three optics tubes. Each tube consists of a window, filter stack, three silicon reimaging optics, a feedhorn array, and finally the detector focal plane. The AdvACT upgrade has already replaced each of ACTPol's three detector arrays, replacing optics tube elements to accommodate different frequency bands where needed. The 2017 season configuration consists of one high-frequency (HF) array, observing at 230 and 150 GHz, and two mid-frequency (MF) arrays, observing at 150 and 90 GHz [3]. The last array of AdvACT to be deployed is the low-frequency (LF) detector array, which will replace one of the MF arrays and observe at 27 and 39 GHz.

Single-frequency observations of the CMB are limited by foregrounds such as synchrotron, spinning dust emission, galactic dust, and dusty star-forming galaxies. AdvACT's high- and low-frequency coverage allows for the removal of these foregrounds, with the low- frequency coverage aiding in the removal of synchrotron and spinning dust emission. The wide frequency coverage (27–230 GHz) and fine angular resolution ($1.4'$ at 150 GHz) of AdvACT will enable a wide range of science such as improving constraints on dark energy, the sum of the neutrino masses, and the existence of primordial gravitational waves [3]. Here we present the characterization of the detector test die used to select the final detector parameters for fabricating the AdvACT LF array.

2 The Detectors

The LF array is a polarization-sensitive dichroic array of 73 pixels coupled to transition edge sensor (TES) bolometers [4]. Each pixel has four orthomode transducer (OMT) coupling probes, two for each linear polarization, connected to superconducting niobium microstrip lines that transmit radiation to the AlMn TES bolometers [5,6]. There are four optical TESes per pixel, a pair for each linear polarization at both 27

and 39 GHz, as well as two dark TESes. Each TES island is weakly coupled to the cold bath by a set of four SiN legs. During operation, the TES is voltage-biased to keep it on the superconducting transition, which is designed to be at 165 mK. The geometry of the TES legs determines the thermal conductance to the bath, G, which limits how much power the detector can dissipate before saturating.

The TES leg geometry is selected to optimize the performance under expected loading conditions at the ACT site. This selection is largely driven by the saturation power without optical loading, P_{sat}, and the thermal conductivity, G. The target saturation powers are 1.5 pW at 27 GHz and 7.8 pW at 39 GHz, which corresponds to three times the estimated loading at each frequency. These are much lower saturation powers than those in the MF (12.5 and 11.3 pW) and HF (25 and 12.5 pW) arrays, driving us to much longer leg lengths. However, similarly long legs have been fabricated for SPIDER [7].

The following model is used to describe how P_{sat} is determined by the bath temperature, T_{bath}, and the critical temperature of the device, T_c:

$$P_{sat} = K \left(T_c^n - T_{bath}^n \right).$$
(1)

The thermal conductivity, G, is then given by,

$$G = \frac{d P_{sat}}{dT_c} = nKT_c^{n-1}.$$
(2)

The LF detector test die leg parameters were selected by extrapolating a linear fit to the P_{sat} for the MF and HF detectors as a function of the cross-sectional area to the leg length, A/l. Test dies with several leg variants were then fabricated to explore the parameter space near $P_{sat} = 1.5$ and near $P_{sat} = 7.8$ pW. These variants are shown in Fig. 1. Additional devices with different heat capacities were fabricated to optimize the temporal response of the detector. The detectors must respond quickly enough to
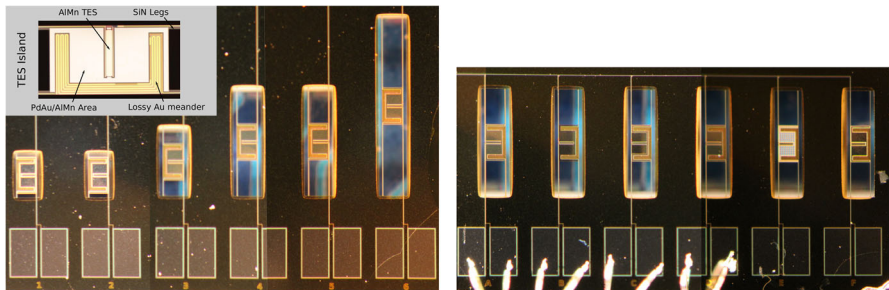

Fig. 1 (Left): LF prototype transition edge sensors with different leg geometries. The devices are labeled 1–6 from left to right. Table 1 lists the design frequency and leg parameters for each of the devices. Inset to this figure in the upper left is a close-up of a single-labeled TES island. (Right): LF prototype TESes with different PdAu/AlMn volumes. The devices are labeled A to F from left to right. Devices A through D have no PdAu, with devices A and D having the full AlMn volume. Device B only has AlMn in the central region that forms the TES, while device C has a reduced area of AlMn. Device F has a full volume of PdAu and AlMn, and device E has a patterned reduction in PdAu, referred to as "swissed" (Color figure online)

Table 1 Measured detector properties

ID	f (GHz)	w (μm)	l (μm)	T_c (mK)	P_{sat} (pW)	G (pW/K)	R_n (mΩ)	n
1	39	14.4	61.0	178.9 ± 0.1	12.5 ± 0.7	276.1 ± 15.5	7.9 ± 0.1	3.4 ± 0.1
2	39	12.1	61.0	178.5 ± 0.2	10.5 ± 0.3	229.3 ± 7.5	7.8 ± 0.1	3.4 ± 0.1
3	27	10.0	219.8	173.4 ± 1.0	4.1 ± 0.2	88.3 ± 4.5	7.5 ± 0.1	3.0 ± 0.1
4	27	10.0	500.0	170.5 ± 1.2	2.1 ± 0.1	44.0 ± 1.7	7.5 ± 0.1	2.8 ± 0.1
5	27	15.0	500.0	172.9 ± 1.9	3.5 ± 0.4	76.5 ± 7.3	7.5 ± 0.1	3.0 ± 0.1
6	27	10.0	1000	164.7 ± 2.5	1.0 ± 0.1	22.6 ± 2.3	7.5 ± 0.1	2.7 ± 0.1

ID corresponds to the device design variations shown in Fig. 1 (Left), f is the design frequency for the detector, w is the TES width, l is the TES leg length, T_c is the critical temperature of the TES, P_{sat} is the saturation power of the detector, G is the thermal conductivity, R_n is the normal resistance, and n is the thermal conductivity exponent. Parameters correspond to a bath temperature of 100 mK, which will be the temperature of the devices in the field. The mean and standard deviation of each parameter for the measured devices are shown. Errors shown do not account for correlation between parameters. Section 3 discusses the correlation between T_c and n
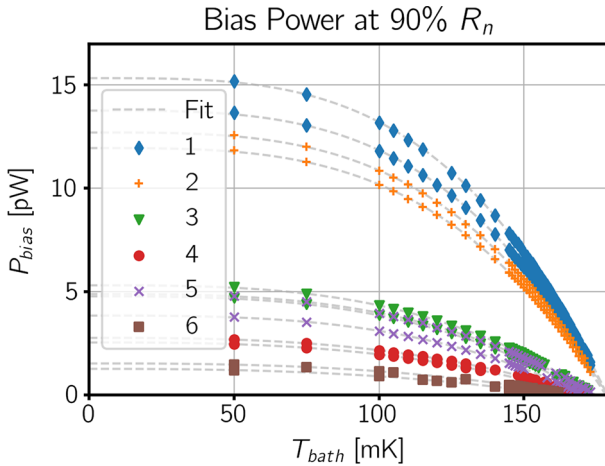
Fig. 2 Bias power at 90% the normal resistance, R_n, as a function of the bath temperature, T_{bath}, for each of the tested prototype TES devices. The upper group, devices 1 and 2, are the 39 GHz devices, while the lower group, devices 3, 4, 5, and 6, are lower saturation power 27 GHz devices. The fit for each individual device is to Eq. (1) (Color figure online)

prevent smearing of the signals from the sky or from the half-wave plate modulators [3], but this must be balanced against the temporal response becoming so fast that the detectors become unstable [8]. Both types of devices were characterized, and the final leg and heat capacity geometries for use on the LF array were selected based on those results.

3 Device Characterization

The optimal TES leg geometries were determined by measuring current–voltage (IV) curves at many different bath temperatures, ranging from 50 to 180 mK. These IV curves are used to determine the bias power required to drive the TES to 90% of the normal resistance, R_n. We define this value to be the saturation power, P_{sat}. The bias powers at 90% R_n for each bath temperature are fit to Eq. (1), as shown in Fig. 2, for K, T_c, and n.

Based on previous measurements of the P_{sat} values for the MF and HF detectors, we expect P_{sat} to be proportional to the ratio of A/l [3]. In Fig. 3, we show the measured P_{sat} versus the ratio of A/L. The black dashed line is the best-fit linear relation, which was used to select the leg geometry of the 39 GHz detectors. For these, we choose to keep the leg length the same as the HF and MF detectors, $l = 61\,\mu\text{m}$, which gave a width, w, of 12.1 μm.

The 27 GHz detectors have the lowest target P_{sat} of all the AdvACT detectors at 1.5 pW. While the test die parameters were selected based on the HF and MF linear fit, we find that the low saturation power, longer leg length detectors differ in their behavior with P_{sat} as a function of A/l in that the slope is larger by about a factor of two. This may be due to the phonon transport differing for the much longer legs. This
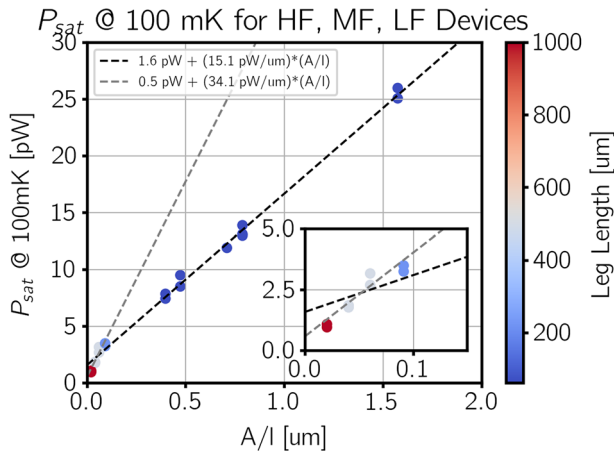
Fig. 3 Plot of P_{sat} versus A/l, where A is the cross-sectional area of one of the four TES legs and l is its length, for typical HF (230/150 GHz), MF (150/90 GHz), and LF (39/27 GHz) devices. The color scale shows the leg length, with all HF, MF and 39 GHz LF legs being 61 μm long, while the LF 27 GHz test devices have a range of longer leg lengths as shown in Table 1. The black dashed line fit is to the HF, MF, and 39 GHz LF detectors. The gray dashed line is a fit to just the 27 GHz LF detectors, which have the lowest saturation power of all the AdvACT detectors, and differs from the trend exhibited by the $l = 61.0$ μm detectors. We allow for a nonzero P_{sat} offset in the fit, which may be present due to residual conductance from the Nb. The inset plot is a zoom in on the low P_{sat} LF detectors (Color figure online)

difference is reflected in the 27 GHz devices having a thermal conductance exponent, n, ≤ 3, compared to $n \sim 3.4$ for the 39 GHz devices, as shown in Table 1. While we do not account for correlation between fit parameters in our error determination in Table 1, we do find there to be a negative correlation between T_c and n, so for a fixed T_c the difference between the 27 and 39 GHz detector n values will persist. We fit the devices with $l > 61$ μm independently, leading to the gray dashed line in Fig. 3, which we used to select the final 27 GHz detector leg parameters of $w = 10$ μm and $l = 628$ μm. Measured prototype device parameters are shown in Table 1. The measured critical temperatures for most of the devices were found to be above the target 165 mK. Selection of the final leg geometries for fabricating the LF array was done after scaling these results to a T_c of 165 mK.

The detector responsivity decreases with increasing frequency due to the thermal time constant of the detector, which can be varied by adding heat capacity to the TES island. We tested six different recipes of PdAu and AlMn, in order to explore how the time constant varied as a function of each materials volume. These six test devices were all 27 GHz devices, four with AlMn volumes ranging from 2639.6 to 36538.4 μm³ and no PdAu, two of which had the same AlMn volume but different leg widths, and two with the full 36538.4 μm³ AlMn volume while having either 21451.8 or 36112.8 μm³ of PdAu. Extrapolations from the previously fabricated MF devices were suitable for the 39 GHz devices.

We report the time constant of the detector as $f_{3dB} = 1/2\pi\tau$, defined as the frequency at which the response of the detector decreases by a factor of two compared to the DC response. The target f_{3dB} for the LF detectors ranges from 81 to 275 Hz
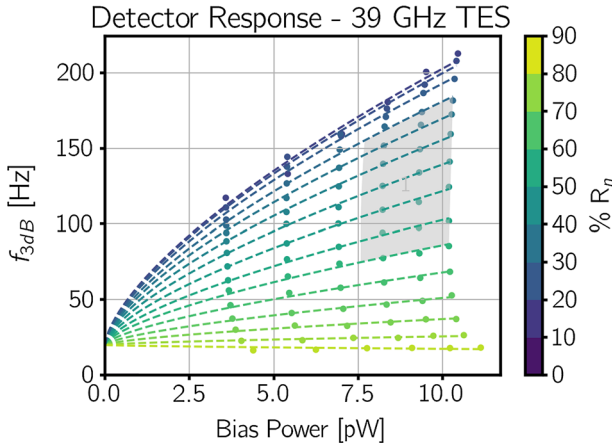
Fig. 4 Bias step results for a single 39 GHz prototype detector. The gray region indicates the targeted operating range of the detector in the field. Each vertical grouping of points is at one bath temperature. The bias point in $\%R_n$ is selected, and then, a square wave is applied. The f_{3dB} is measured from the response to the square wave, and this is repeated for a full range of bias points before moving to the next temperature. These data are used to estimate the detector response speed under a range of optical loading conditions in the field (Color figure online)

for 35–70% R_n across the range of expected bias powers under loading in the field. This range is set by requiring fast enough detectors to observe with a rapidly rotating half-wave plate modulator, but not too fast that they could become unstable [3].

We test the response time by adding a small square wave to the voltage bias applied to the detectors with amplitude ranging from 1 to 5% of the DC bias value. The response is sampled at 250 kHz to measure the exponential fall time of the detector current, or τ. We do this at six different bath temperatures and several different points on the TES transition, measured by the TES resistance relative to normal, $\%R_n$, as shown in Fig. 4. These data are then fit to a two-fluid model described by Eq. (3), where A and B are a function of measurable parameters specified in [9], and P_{bias} is the bias power,

$$f_{3dB} = A + B P_{bias}^{2/3}. \tag{3}$$

This model qualitatively captures the data, though a linear model yields similar results. A better understanding of the TES behavior and physics throughout the transition is work in progress.

From these data, we found that having PdAu on the 27 GHz devices, in addition to the full AlMn volume, decreased the f_{3dB} below our target threshold of 81 Hz. Based on this, we chose to have 73% of the full (largest tested) AlMn volume (full being 36538.4 μm^3) and no PdAu on the 27 GHz detectors and 100% of the full AlMn volume and 76% of the full volume of PdAu (full being 36112.8 μm^3) for the 39 GHz detectors.

4 Readout

The LF array will have a much smaller number of TESes than AdvACT's HF and MF arrays, but it will be read out using the same time- division multiplexing (TDM) scheme [3,10–12]. Each TES in the LF array will be voltage-biased and multiplexed through the warm Multi-Channel Electronics (MCE) using a SQUID-based TDM architecture developed at NIST/Boulder [13,14]. Containing fewer pixels, the LF cold electronics will be a simplified adaptation of the HF and MF designs, using the same PCB used in the HF and MF arrays. The LF array will have a multiplexing (MUX) factor, or number of detectors per readout channel, of 26:1, whereas HF and MF have MUX factors of 64:1 and 55:1, respectively. The cold readout electronics are similar otherwise to the electronics described in [3,10].

The LF array readout wiring has been designed such that TESes from polarization pairs at one optical frequency are read out on the same column and thus the same 1 K SQUID series array and 300 K warm amplifier. Unlike in the MF and HF arrays, each column in the LF array has its own dedicated TES bias line and dark TESes are wired to their own column. This is an improvement over the MF and HF readout because each detector type (27, 39 GHz, and dark), which will have different optimal bias powers, can be independently biased. Deliberate shorts on some unused shunt inputs have also been implemented, providing Johnson noise channels for independently probing detector bias line noise.

5 Conclusion

We fully characterized new test dies, which were designed to demonstrate the low P_{sat} values needed to optimize the LF array. The LF cryogenic readout electronics have been assembled and tested. The LF detector array is currently being fabricated at NIST and will be deployed to extend the range of AdvACT from 27 to 230 GHz.

This demonstrates our ability to cover a wide range of saturation powers (as low as 1 pW) and detector response speeds through modification of the detector leg length, the leg width, the AlMn volume, and the PdAu volume on a single-detector design. This has direct application to detector design for future CMB experiments, such as the Simons Observatory and CMB-S4, which will face similar design challenges.

References

1. R.J. Thornton et al., ApJS **227**, 21 (2016). https://doi.org/10.3847/1538-4365/227/2/21
2. J.W. Fowler et al., Appl. Opt. **46**(17), 3444 (2007). https://doi.org/10.1364/AO.46.003444
3. S.W. Henderson et al., J. Low Temp. Phys. **184**(3), 772 (2016). https://doi.org/10.1007/s10909-016-1575-z
4. S.M. Simon et al., J. Low Temp. Phys. This Special Issue (2018)
5. D. Li et al., J. Low Temp. Phys. **184**(1), 66 (2016). https://doi.org/10.1007/s10909-016-1526-8

6. S.M. Duff. et al., J. Low Temp. Phys. This Special Issue (2018)
7. J.P. Filippini et al., in *Millimeter, Submillimeter, and Far-Infrared Detectors and Instrumentation for Astronomy V, Volume 7741 of Proceedings of SPIE* (2010), p. 77411N. https://doi.org/10.1117/12.857720
8. K. Irwin, G. Hilton, *Transition-Edge Sensors* (Springer, Berlin, 2005), pp. 63–150
9. K.D. Irwin et al., J. Appl. Phys. **83**(8), 3978 (1998). https://doi.org/10.1063/1.367153
10. S.W. Henderson et al., in *Millimeter, Submillimeter, and Far-Infrared Detectors and Instrumentation for Astronomy VIII, Volume 9914 of Proceedings of SPIE* (2016), pp. 99141G. https://doi.org/10.1117/12.2233895
11. K. Crowley et al., J. Low Temp. Phys. This Special Issue (2018)
12. S.K. Choi et al., J. Low Temp. Phys. This Special Issue (2018)
13. E.S. Battistelli et al., J. Low Temp. Phys. **151**, 908 (2008). https://doi.org/10.1007/s10909-008-9772-z
14. J. Beyer, D. Drung, Supercond. Sci. Technol. **21**(10), 105022 (2008). https://doi.org/10.1088/0953-2048/21/10/105022